The effect of phosphine in syngas on Ni–YSZ anode-supported solid oxide fuel cells

Chunchuan Xu [a,*], John W. Zondlo [a], Harry O. Finklea [b,d], Oktay Demircan [b], Mingyang Gong [c], XingBo Liu [c]

[a] Department of Chemical Engineering, West Virginia University, Morgantown, WV 26506, USA
[b] C. Eugene Bennett Department of Chemistry, West Virginia University, Morgantown, WV 26506, USA
[c] Department of Mechanical & Aerospace Engineering, West Virginia University, Morgantown, WV 26506, USA
[d] National Energy Technology Laboratory-Institute for Advanced Energy Studies, US Department of Energy, USA

ARTICLE INFO

ABSTRACT

Ni–YSZ cermet is commonly used as the anode of a solid oxide fuel cell (SOFC) because it has excellent electrochemical performance, not only in hydrogen fuel, but also in a clean blended synthetic coal syngas mixture (30% H_2, 26% H_2O, 23% CO, and 21% CO_2). However, trace impurities, such as phosphine (PH_3), in coal-derived syngas can cause degradation in cell performance [J.P. Trembly, R.S. Gemmen, D.J. Bayless, J. Power Sources 163 (2007) 986–996]. A commercial solid oxide fuel cell was exposed to a syngas with 10 ppm PH_3 under a constant current load at 800 °C and its performance was evaluated periodically using electrochemical methods. The central part of the anode was exposed directly to the syngas without an intervening current collector. Post-mortem analyses of the SOFC anode were performed using Raman spectroscopy, X-ray diffraction (XRD), scanning electron microscopy (SEM), energy dispersive spectroscopy (EDS) and X-ray photoelectron spectroscopy (XPS). The results show that the impurity PH_3 caused a significant loss of the Ni–YSZ anode electrochemical performance and an irreversible Ni–YSZ structural modification. Ni_5P_2 was confirmed to be produced on the cell surface as the dominant nickel phosphorus phase.

© 2009 Elsevier B.V. All rights reserved.

1. Introduction

The standard SOFC composition, Ni–YSZ cermet anode plus YSZ electrolyte plus $LaSrMnO_3$ cathode, can directly use coal syngas because of its ability to tolerate the CO and CO_2 which are present in coal-derived syngas. There is substantial interest in the effects of gaseous impurities contained in syngas on the long-term performance of SOFCs [2]. Besides sulfur, thermodynamic calculations suggest the presence of volatile impurities containing P, As, Sb, Se, Cd, Pb, and Hg in warm syngas [1]. This paper focuses on the phosphorus impurities. Volatile forms of phosphorus under warm gas cleanup conditions include PH_3 and phosphorus oxides [1].

Several researchers have reported the effects of phosphine in syngas mixtures on Ni–YSZ anodes. Ni_5P_2 was produced on the Ni–YSZ anode surface in the PH_3 testing reported by Trembly [3]. Pederson et al. observed a delay in the degradation of cell performance upon exposure to 2–5 ppm PH_3, and also noted the formation of nickel phosphide phases on the nickel metal current collector and in the Ni/YSZ composite anode. Degradation was

assigned to changes in the current collector [4]. Zhi et al. exposed Ni/YSZ half cells to a high concentration of PH_3 (20 ppm). Post-mortem analyses by X-ray diffraction indicated the presence of nickel phosphate and zirconyl phosphate phases [5].

In this paper, we report extended testing of commercial button cells with Ni/YSZ composite anodes in a syngas mixture containing 10 ppm PH_3. The current collector is arranged to expose the central part of the anode to the fuel gas mixture without any intervening metal grid or metal paste. Periodic evaluation of impedance is used to follow the ohmic and polarization resistances during the experiment. Extensive post-mortem analyses by SEM, X-ray diffraction, Raman spectroscopy and XPS are used to evaluate chemical and microstructural changes in the anode. These results are compared to the previous reports and to thermodynamic predictions. The most striking observation is extensive migration of nickel to the anode surface and into large pores in the anode.

2. Experimental methods

2.1. SOFC composition and testing

In this study, commercial anode-supported solid oxide button cells manufactured by Materials and Systems Research Inc. (MSRI) were used. The cells consisted of five layers: (1) 0.8–0.9 mm thick
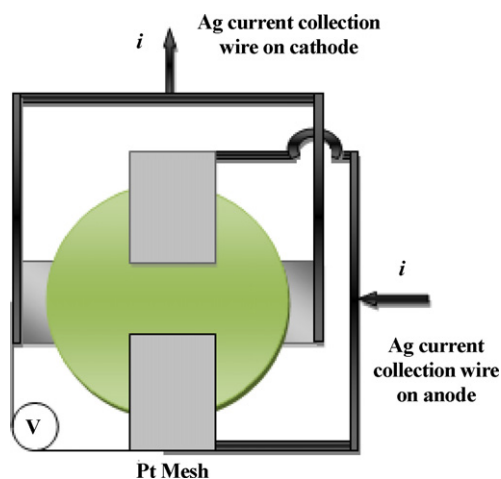
Fig. 1. Button cell contact configuration.

Ni–8YSZ layer which supports the cell structure, (2) 25-μm thick highly catalytic Ni–8YSZ mixture interlayer, (3) 20-μm thick 8YSZ (YSZ) electrolyte, (4) 25-μm thick $La_{0.8}Sr_{0.2}MnO_3$ (LSM)-8YSZ interlayer, and (5) 50-μm thick current-collection layer made of LSM. The cell effective area (cathode area) is 2 cm^2 [6]. A platinum current-collection mesh was attached to the cell cathode using platinum paint. A pair of platinum current-collection meshes separated by 0.5 cm was symmetrically attached on the cell anode using nickel paste. The anode center was directly exposed to the injected fuel without any intervening current collector or metal paste so that the impurity effects on the cell anode can be directly observed and identified (Fig. 1). The two ends of the cathode and two ends of the anode current-collection meshes were connected by thick silver wires; two thin voltage-sensing wires were connected to the cathode and anode current-collection meshes. Pure nickel and YSZ coupons were placed on the Pt meshes of the anode to serve as passive reactants for the phosphine. The SOFC was mounted between two alumina flanges using mica washers as the sealing material. For all tests, the button cell assembly was mounted in a furnace operated at 800 °C. Alicat Scientific mass flow controllers (MFCs) were used to control the fuel and air stream flow rates and compositions. MFCs were used to control the flow rates of H_2, H_2O, CO, CO_2, N_2/PH_3 (1000 ppm PH_3 in nitrogen) and air separately. A temperature-controlled humidifier was used to adjust the H_2O concentration of the simulated coal syngas provided to the anode. The total syngas fuel flow rate was kept at approximately 200 ± 2 sccm (standard cubic centimeters per minute) and the air-flow rate was kept at approximately 300 ± 2 sccm. The anode fuel transfer lines were pre-heated to prevent water condensation between the humidifier and furnace. CO, CO_2 and PH_3 were injected downstream of the anode humidifier close to furnace to ensure all trace species injected into the stream reached the anode of the SOFC.

2.2. Electrochemical testing of SOFC

The "as-received" SOFC was heated from room temperature to 800 °C at a rate of 7 °C min^{-1}. During the heating period, the anode was provided 100 sccm of N_2 and the cathode was provided 100 sccm of air. Once the SOFC reached 800 °C, the anode of the button cell was reduced by providing fuel flow containing 10% H_2 and the balance N_2 for approximately 2 h. After this time, 50% H_2 and 50% N_2 were fed for another hour in order to complete the reduction. The cell open circuit voltage was stable 1.061 ± 0.001 V with humidified H_2 (3% H_2O) as the fuel. The open circuit voltage (OCV) was less than theoretical value of 1.100 V with 97% H_2, 3% H_2O on the anode side and air (21% O_2) on the cathode side pre-

sumably because of slight leakage around the cell seals and possibly through the electrolyte. Then, 0.25 A cm^{-2} direct current (DC) was loaded for a current treatment overnight (14 h). The constant DC current density load was supplied by a solid-state loaded cell (TDI Transistor Device SD-103). After loading the SOFC at constant current density 0.5 A cm^{-2} for another 24 h, the cell voltage stabilized at 0.715 ± 0.001 V. Upon shifting to syngas fuel (nominal concentration 30% H_2, 26% H_2O, 23% CO, and 21% CO_2), the cell OCV decreased to 0.962 ± 0.002 V. After the cell voltage stabilized at 0.611 ± 0.003 V under a loading current density of 0.5 A cm^{-2} for 26 h, 10 ppm PH_3 was injected in the fuel stream. The cell polarization curve and impedance spectra were taken at 0 h, 46 h, 100 h, 160 h and 250 h after adding PH_3. The impedance spectra were collected using a Solartron SI 1260 impedance/gain-phase analyzer with AC amplitude of 20 mV at frequencies ranging from 100 kHz to 0.1 Hz. After exposure to syngas with 10 ppm PH_3 for 250 h, the anode side of cell was purged with N_2 and cooled down from 800 °C to room temperature in about 3 h still under the N_2 purge. To check the reversibility of poisoning effects of PH_3, one of the PH_3-poisoned cells was run under the same conditions except that the fuel was changed to H_2 for 12 h after the prolonged exposure to PH_3-contaminated syngas. The loss of performance of cell was not reversed, but the cell did not continually degrade.

2.3. Morphology and structural analysis

The surface and cross-section microstructure of the cell anode were examined with a Hitachi S-4700 SEM with EDS. To determine the composition of the anode, XRD (Panalytical X'Pert PM-3040 PRO) system, Raman microscope (HORIBA LabRAM ARAMIS, 532 nm laser) and XPS (PHI 5000 VerasProbe XPS Microprobe) were employed. Thermodynamic analysis is carried out with a FACTSAGE 5.4 software package to predict the predominant phase diagram under cell operating condition by calculating the minimum Gibbs free energy change of the defined reactions.

3. Experimental results

3.1. Polarization curves and impedance spectra

After accounting for slight increases in cell performance during burn-in, the SOFC performance (voltage at a constant current density) is stable over 24 h in coal syngas. The cell performance degrades immediately upon introduction of PH_3 (Fig. 2). Performance loss is seen at nearly all current densities (Fig. 3). At a
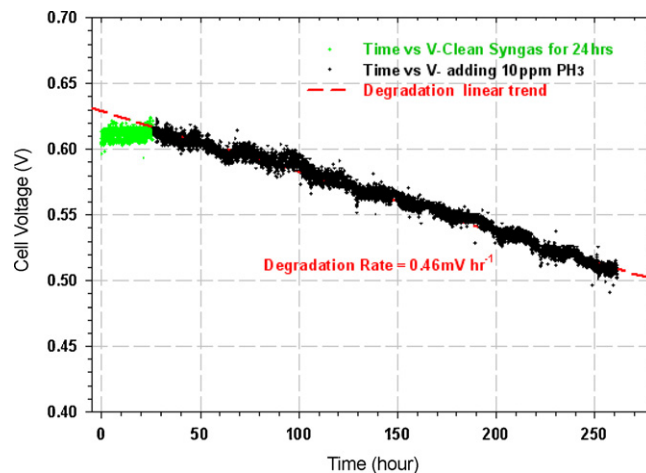

Fig. 2. The cell voltage versus time under load 0.5 A cm^{-2} operating on syngas before and after adding 10 ppm PH_3 at 800 °C.
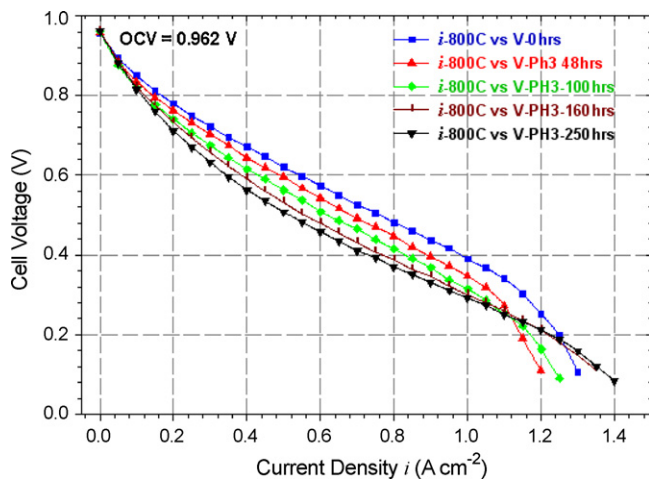
Fig. 3. The polarization curves of Ni–YSZ anode-supported button cell during exposure to syngas before and during addition of 10 ppm PH₃ at 800 °C.

Fig. 5. The cell ohmic resistance R_Ω and polarization resistance R_p versus time after adding 10 ppm PH₃.

constant current load of 0.5 A cm^{-2}, the cell voltage degradation rate is a constant 0.46 mV h^{-1} (Fig. 2). The cell OCV consistently remains at 0.962 V. The dominant anodic process is assumed to be H₂ oxidation, with the CO consumed by the water–gas shift equilibrium [7]. At the diffusion limited region near zero cell voltage, the cell current density initially decreases, but increases after exposure to 10 ppm PH₃ for 100 h (Fig. 3). This abnormal behavior is unexpected, since the cell concentration polarization should increase with degradation of the cell. Three separate MSRI cells have been tested, and all three tests showed the same abnormal trend.

The impedance spectra under a DC bias of 0.662 V shows that the ohmic resistance R_Ω (high frequency intercept with Z' axis) and the total polarization resistance R_{total} (low frequency intercept with Z'' axis) increase with increasing time of exposure to PH₃ (Fig. 4). Before adding PH₃, the cell ohmic resistance and total polarization resistance (area specific resistance) are about 0.22 Ω cm^2 and 0.55 Ω cm^2. After adding PH₃ for 250 h, they are 0.325 Ω cm^2 and 0.88 Ω cm^2, respectively. The difference between R_{total} and R_Ω is the polarization resistance R_p which is associated with activation and concentration polarization effects. These resistances increase in linearly with time (Fig. 5). The R_{total} increase rate is 1.29 mΩ cm^2 h^{-1} which is three times the R_Ω increase rate of 0.42 mΩ cm^2 h^{-1}. The polarization resistance R_p increase rate is about 0.87 mΩ cm^2 h^{-1}.

3.2. SEM micrograph and EDS spectra

Photographs of a clean reduced cell and the post-mortem cell anode are shown in Fig. 6. In the post-mortem picture (Fig. 6(b)), a colored oval pattern at the center of the anode has appeared just under the quarter-inch alumina fuel inlet tubing. The exposed anode surface area is metallic in appearance, which implies a change of Ni–YSZ composition and pore structure.

An SEM image of the anode surface after prolonged exposure to 10 ppm PH₃ is shown in Fig. 7(a). For comparison, the outer surface of a reduced anode never exposed to PH₃ is provided in Fig. 7(b). The poisoned anode surface shows significant losses of pore structure and agglomeration of material on the open surface area.

The cross-section image in Fig. 8(a) shows that the Ni has migrated to the top surface to become a layer while Ni particles are fused together in big chunks in the pores. Ni weight concentrations by EDS spectra scan are given at the five spots. The Ni weight concentration is 86% at spot No. 1 on the top layer, which is much higher than that of clean reduced anode (60–63%). The low Ni weight concentration 18% at spot No. 2 is just under the top layer. The No. 3 and 5 spots are composed of 59% and 56% nickel, respectively, which is consistent with untreated anode. Spot No. 4 (83% Ni) appears to be a nickel chunk formed in a former cavity. Similar morphological changes of Ni–YSZ anode after PH₃ exposure have been found in the previous study [4,8]. However, this study uses an anode with an open center directly exposed to the contaminant downstream. Consequently, the Ni migration in anode and to the anode surface is clearly independent of the current-collection mesh cover. The cross-section image of the clean reduced anode in Fig. 8(b) displays the same porous Ni–YSZ matrix as the anode surface image in Fig. 7(b). There are no Ni chunks evident in the clean anode like those in the PH₃-poisoned cell image in Fig. 8(a). In the larger scale view of the cell cross-section in Fig. 9(a), the microstructure of the top 200–300 μm depth around the cell center is significantly reconstructed by exposure to PH₃. In the very top layer, the pore structure has all but vanished. Compared to the clean reduced cell anode cross-section image (Fig. 9(b)), the reconstruction effect by PH₃ impurity can be clearly identified. The greater depth of structural change coincides with the current lines at the cell center.

The EDS spectra (Fig. 10(a and b)) show the change of the composition on the anode surfaces of a clean reduced anode and the PH₃ poisoned anode, respectively. The nickel peak at 0.860 keV becomes much stronger relative to the overlapping Y and Zr peaks after the cell anode is exposed to PH₃. Deconvolution of the peak at 2.02 keV
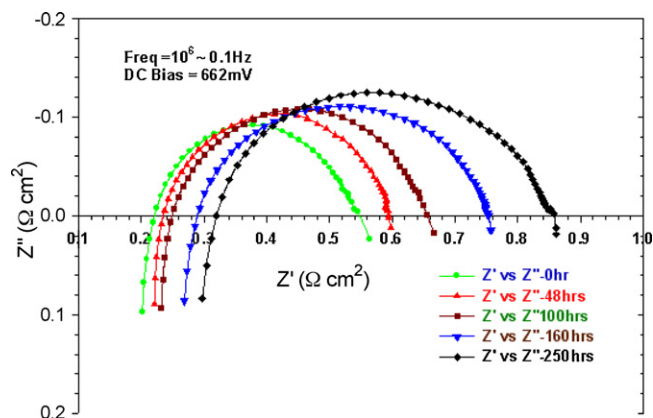

Fig. 4. The normalized impedance spectrum of Ni–YSZ anode-supported button cell during exposure to syngas before and during exposure to 10 ppm PH₃ at 800 °C.
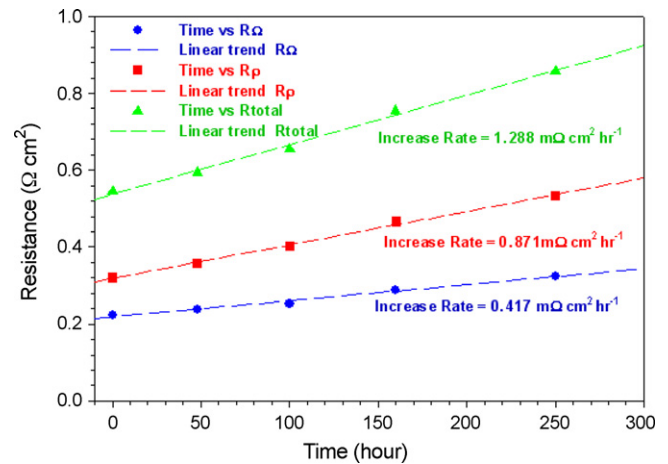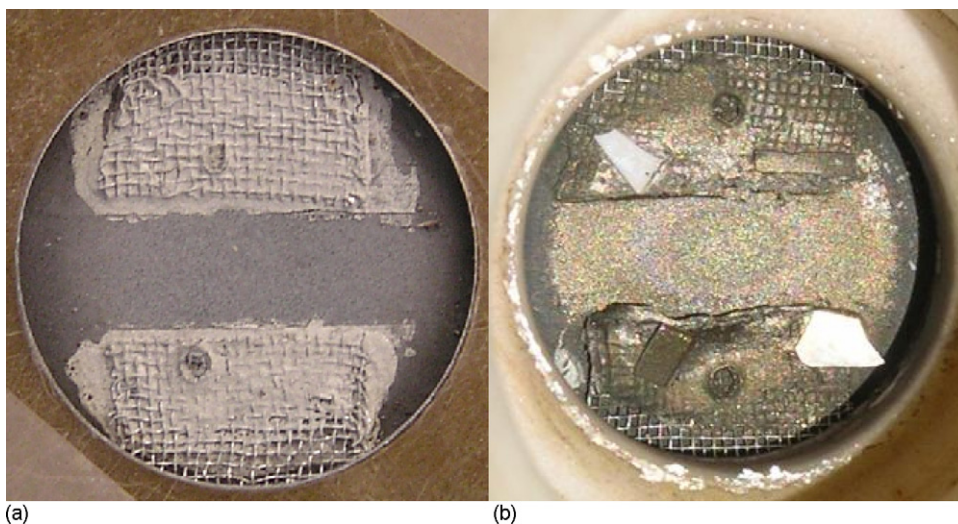
Fig. 6. (a) Clean reduced cell anode and (b) post-mortem PH_3-poisoned cell anode side image.
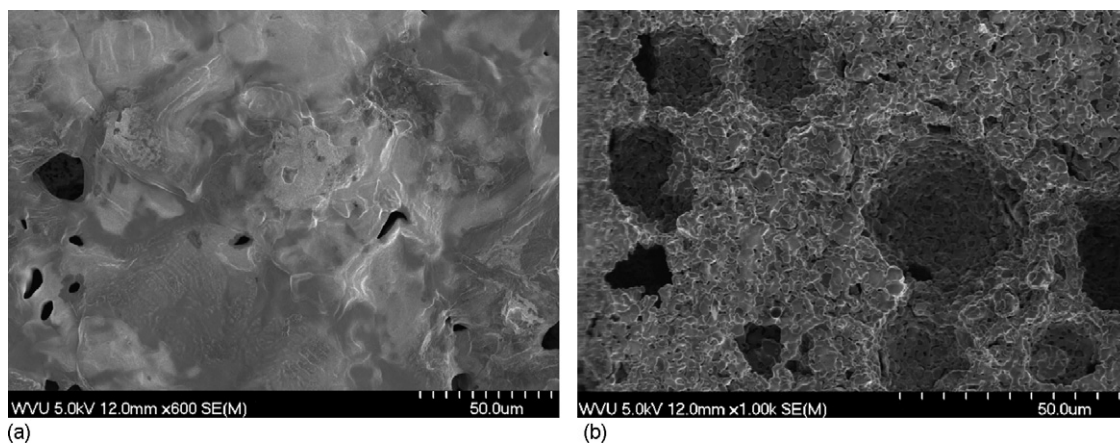

Fig. 7. (a) The cell anode surface SEM micrograph after exposure to syngas with 10 ppm for 250 h and (b) the clean reduced cell anode surface SEM micrograph for comparison.

suggests that phosphorous is present on the surface. The carbon signal is not significant for both of spectra which indicate that the syngas composition used in these experiments does not result in much coke or carbon contamination on the Ni–YSZ anode.

These data clearly indicate that nickel migrates to the outer surface of the anode and that nickel particles are redistributed inside the anode upon exposure to PH_3. The redistribution of nickel affects multiple parameters important to the performance of the anode, such as the triple phase boundary (TPB) length, fuel H_2 reaction area, pore size, porosity and tortuosity. These microstructural reconstructions appear to be irreversible.
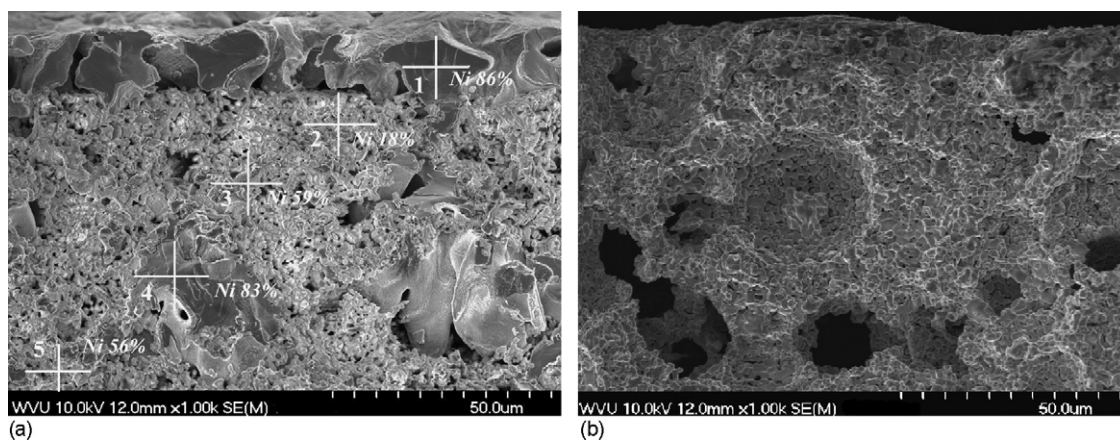

Fig. 8. (a) The top 50 μm cell anode cross-section SEM micrograph after exposure to syngas with 10 ppm PH_3 for 250 h. EDS scan shows the Ni wt.% on five different spots and (b) the top 50 μm clean reduced cell anode cross-section SEM micrograph for comparison.
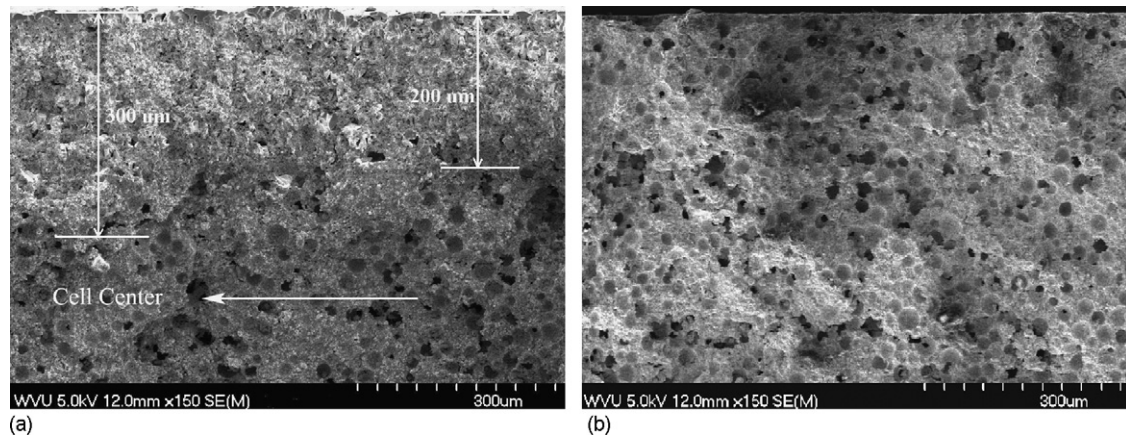
Fig. 9. (a) The top 500 μm cell anode cross-section SEM micrograph after exposure to syngas with 10 ppm PH$_3$ for 250 h and (b) the top 500 μm clean reduced cell anode cross-section SEM micrograph for comparison.
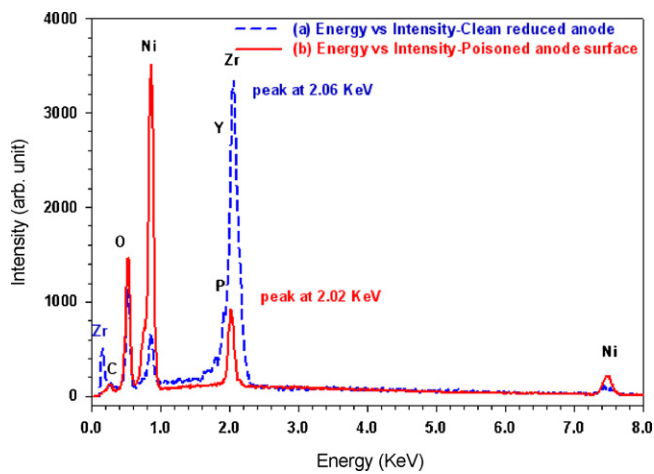

Fig. 10. The EDS spectra of the clean reduced Ni–YSZ anode surface (dash line) and the Ni–YSZ anode surface after exposure to PH$_3$ for 250 h (solid line).
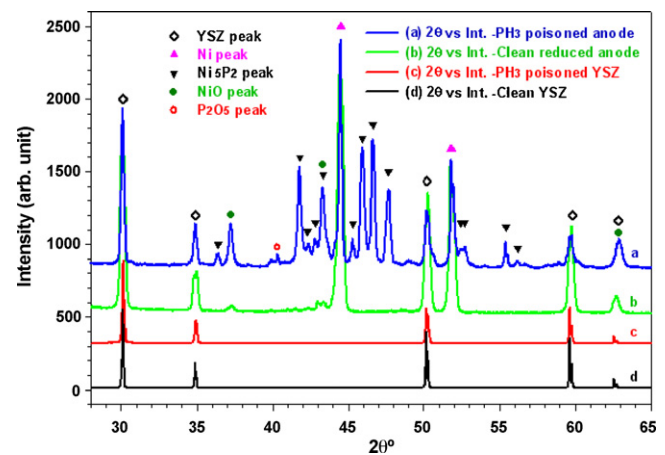

Fig. 11. XRD spectra of Ni–YSZ anode supported cell surfaces. Ni$_5$P$_2$ was confirmed to be present on the anode surface of cell after exposure to syngas with 10 ppm PH$_3$.

3.3. XRD and Raman spectra

The evidence for nickel phosphide compounds on the PH$_3$-poisoned Ni–YSZ anode center is provided by XRD spectra in Fig. 11(a and b). The peak positions of YSZ, Ni$_5$P$_2$, Ni, NiO and P$_2$O$_5$ are listed in Table 1 by 2θ locations [9–13]. Both spectra in Fig. 11(a) and (b) of Ni–YSZ anode have YSZ, Ni and NiO peaks. There are a group of Ni$_5$P$_2$ peaks on the PH$_3$-poisoned Ni–YSZ anode spectrum (Fig. 11(a)). The other nickel phosphide peaks, such as Ni$_3$P, Ni$_8$P$_3$ and Ni$_{12}$P$_5$ [22], may overlap with the peaks of Ni$_5$P$_2$. However, two of the signature peaks of Ni$_5$P$_2$ at 45.95° and 47.66 ± 0.02° appear in the spectrum (Fig. 11(a)) [10], so Ni$_5$P$_2$ is assumed to be the dominant phase. There is a weak peak at 40.31 ± 0.02°, which could be one of P$_2$O$_5$ main peaks [13]. The clean, reduced Ni–YSZ

anode spectrum (Fig. 11(b)) only shows the YSZ, Ni and NiO peaks, and does not exhibit any nickel phosphide peaks. The five signature peaks of YSZ at 2θ values of 30.10°, 34.89°, 50.21°, 59.79° and 62.59 ± 0.02° [9] are displayed on both the YSZ coupon (Fig. 11(c)) and the clean YSZ sample (Fig. 11(d)) spectra. Previously published studies have found specific cell operating conditions as well as the experimental set-up greatly influence the reactions of phosphorus species in syngas with the Ni–YSZ anode and the corresponding product phases. For example it was determined by thermodynamic equilibrium calculation that, for 2 ppm PH$_3$ in syngas, Ni$_5$P$_2$ would most likely form at the inlet of Ni–YSZ anode [1]. Marina et al. conducted a recent experimental study on a Ni–YSZ anode supported cell, and reported formation of Ni$_3$P on both anode surface layer and the Ni grid current collector covering the anode surface exposed

Table 1
XRD peak list 2θ°.

YSZ peaks [9]	Ni$_5$P$_2$ peaks [10]	Ni peaks [11]	NiO peaks [12]	P$_2$O$_5$ peaks [13]
30.10°	36.40°, 41.78°	44.17°	37.24°	40.31°
34.89°	42.36°, 42.83°	51.49°	43.27°	46.53°[a]
50.21°	43.32°, 45.30°		62.59°	
59.79°	45.95°, 46.62°			
62.86°	46.62°, 47.66°			
	52.44°, 52.73°			
	55.43°, 56.14°			
	56.21°			

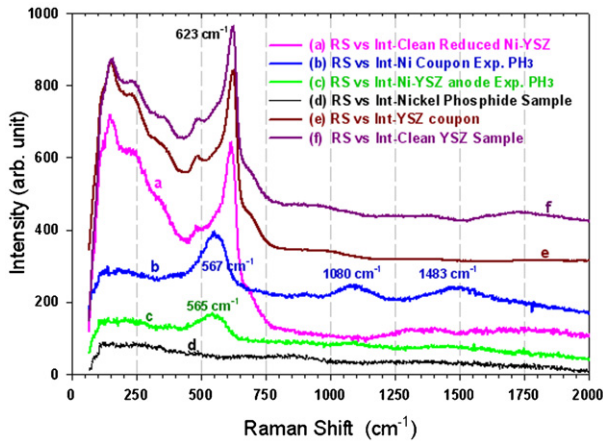[a] The peak may hide in the other peaks.

Fig. 12. Raman spectra of (a) a clean reduced Ni–YSZ anode, (b) a Ni coupon, (c) a PH$_3$-poisoned Ni–YSZ anode, (d) a nickel phosphide sample, (e) a YSZ coupon after exposure to 10 ppm PH$_3$ for 250 h, and (f) a fresh clean YSZ sample.

Fig. 13. XPS spectrum of Ni–YSZ anode exposure to syngas with 10 ppm PH$_3$ for 250 h.

to 2 ppm PH$_3$ in syngas of a similar composition in this study [8]. Despite the prior achievements, the degradation mechanism for the SOFC anode by phosphine attack at real operation conditions is still needed to be clarified from both theoretical and experimental ends. Detailed thermodynamic equilibrium calculation is thus performed (see Section 4.2) to further analyze the current XRD results and elucidate the phase-transition history for Ni–YSZ and its effect on the structural failure of the anode.

The Raman shift spectrum of the clean reduced Ni–YSZ anode surface has the typical YSZ polycrystalline Raman shift peak at $623 \pm 5\,\text{cm}^{-1}$ (Fig. 12(a)) [14]. Also shown are the Raman shift spectra of a Ni coupon (Fig. 12(b)), and a PH$_3$-poisoned Ni–YSZ anode surface center (Fig. 12(c)), both of which show the three NiO Raman shift signature modes at about $560\,\text{cm}^{-1}$, $1080\,\text{cm}^{-1}$ and $1480 \pm 5\,\text{cm}^{-1}$ [15]. The missing YSZ Raman peak in the spectrum for the PH$_3$-poisoned Ni–YSZ anode provides additional evidence that Ni and Ni compounds (possibly NiO and nickel phosphides) cover the top Ni–YSZ anode surface. There is no significant nickel phosphide mode in the Raman shift region between $60\,\text{cm}^{-1}$ and $2000\,\text{cm}^{-1}$ (Fig. 12(d)) [16]. Both the Raman spectra (Fig. 12(e and f)) and the XRD spectra (Fig. 11(c and d)) of the YSZ coupon and a fresh clean YSZ sample are identical, suggesting that the PH$_3$ does not attack YSZ during 250 h exposure in syngas at 800 °C, in contradiction to an earlier report [5].

3.4. XPS spectrum

The XPS spectrum of the Ni–YSZ anode exposed to syngas with 10 ppm PH$_3$ for 250 h is shown in Fig. 13. The major core level detected peaks are phosphorus 2s, 2p, carbon 1s, oxygen 1s, nickel 3p and LMM. The phosphorus 2p 3/2 electron binding energy peak is positioned at 134.30 ± 0.05 eV which implies that the phosphate phase, P$_2$O$_5$ or PO$_4{}^{3-}$, could be present on the sample surface. Ni 2p 3/2 electron has two peaks at 854.60 ± 0.05 eV and 856.80 ± 0.05 eV which could be assigned to nickel oxide, nickel phosphate or nickel hydroxide [17,18]. It should be noted that there are no significant YSZ peaks in the spectrum because the nickel and nickel compounds have covered the surface.

4. Discussion

4.1. Cell degradation electrochemical analysis

By means of electrochemical impedance spectra measurements, the degradation of cell performance can be basically explained by
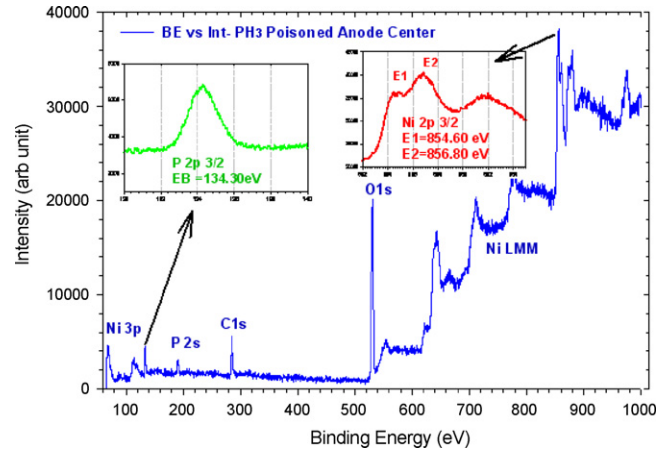
the increasing ohmic resistance R_Ω and polarization resistance R_p. Our testing experience suggests that the resistances associated with the cathode, electrolyte and current collectors contact on the anode remain constant during 250 h of this experiment. Because PH$_3$ was only applied to the anode, the total polarization resistance increase is caused by the increase of ohmic resistance and polarization resistance related to the cell Ni–YSZ anode. Under this assumption, the change of series resistance ΔR_Ω can be due to the changes of anode electronic ohmic resistances ΔR_Ω^a. The increase of polarization resistance ΔR_p can be caused by the changes of concentration polarization at the anode ΔR_{conc}^a and the change of activation polarization at the anode ΔR_{act}^a. The change of total polarization ΔR_{total} can be expressed as

$$\Delta R_{total} = \Delta R_\Omega + \Delta R_p = \Delta R_\Omega^a + \Delta R_{conc}^a + \Delta R_{act}^a \quad \text{or}$$

$$\Delta \eta_{total} = \Delta \eta_\Omega^a + \Delta \eta_{conc}^a + \Delta \eta_{act}^a \tag{1}$$

where $\Delta \eta_\Omega^a$, $\Delta \eta_{conc}^a$ and $\Delta \eta_{act}^a$ are the changes of anode ohmic, concentration and activation polarization.

For the ohmic polarization portion, η_Ω^a depends upon the Ni–YSZ anode and interlayer thickness, the concentration of the Ni in the anode cermet, the porosity, Ni particle size and the particular geometry of the particle-to-particle contact of each phase [6]. The migration of nickel in the anode can cause a non-uniform distribution of nickel particles which could lead to the significant increase of the electronic resistivity of both the anode and anode active layer.

The dominant anodic process is assumed to be H$_2$ oxidation [7]. For the concentration polarization portion, η_{conc}^a is related to the Ni–YSZ anode microstructure, H$_2$ and H$_2$O partial pressure and load current density i. η_{conc}^a can be expressed by Eq. (2) [19]:

$$\eta_{conc}^a = \frac{RT}{2F}\ln\left(1 + \frac{iP_{\text{H}_2}^0}{i_{as}P_{\text{H}_2\text{O}}^0}\right) - \frac{RT}{2F}\ln\left(1 - \frac{i}{i_{as}}\right) \tag{2}$$

where $P_{\text{H}_2}^0$ and $P_{\text{H}_2\text{O}}^0$ are the initial partial pressure of H$_2$ and H$_2$O at anode outer surface, which here are constant. R is the ideal gas constant, F is Faraday constant, T is temperature (K) and i cell working current density. i_{as} is anode-limiting current density which can be expressed as

$$i_{as} = \left(\frac{V_v^a \cdot D_{\text{H}_2,\text{H}_2\text{O}}}{\tau_a}\right)\left(\frac{2F}{RT}\right)\left(\frac{P_{\text{H}_2}^0}{l_a}\right) \tag{3}$$

here $D_{\text{H}_2,\text{H}_2\text{O}}$ is the fuel H$_2$ and H$_2$O binary diffusivity, V_v^a is anode porosity, τ_a is anode tortuosity and l_a is the thickness of anode. The change of anode microstructure will change i_{as} which not only

affects η_{conc}^a but also the curvature of the polarization curve [19]:

$$\frac{d^2\eta_{conc}^a}{di^2} = -\frac{RT}{2F}\left\{\frac{1}{(i_{as}-i)^2} - \left(\frac{P_{H_2}^0}{P_{H_2O}^0 i_{as} + P_{H_2}^0 i}\right)^2\right\} \qquad (4)$$

If Eq. (4) is set to zero, then the current density i^* at the inflexion point on the polarization curve can be solved as

$$i^* = \frac{P_{H_2}^0 - P_{H_2O}^0}{2P_{H_2}^0}i_{as} \qquad (5)$$

During the test, the cell current density slightly increased at the diffusion limited region near zero cell voltage after exposure to 10 ppm PH₃ for 100 h (Fig. 3). The inflexion point on polarization curve shifted toward higher loading current density i, which means that i_{as} was increased after exposure to PH₃ for 100 h. The cell concentration polarization η_{conc}^a had a decreasing tendency according to Eq. (2). Because the gain of i is very small (Fig. 3), the contribution of concentration polarization η_{conc}^a to the change of cell polarization $\Delta\eta_{total}^a$ may not significant at the cell loading current $I = 0.5\,A\,cm^{-2}$. From the post-mortem micrographs (Figs. 9 and 11), the porosity V_ν^a decrease can be clearly seen at the top anode layer. Normally, the porosity V_ν^a and tortuosity τ_a are related proportionally. So limiting current density i_{as} should decrease with decreasing the porosity V_ν^a and increasing tortuosity τ_a which results in the increase of η_{conc}^a. Under actual cell working conditions, one possible explanation of increasing i_{as} could be, the presence of a liquid phase in the anode (see Section 4.2) which could improve the fuel diffusion processes. The anode-limiting current density i_{as} may be enhanced by the increased net effect of the anode porosity, tortuosity and binary diffusivity which leads to a decrease of the concentration polarization η_{conc}^a. To understand this abnormal behavior, further in situ investigation is needed.

For the activation polarization portion, η_{act}^a is related to the Ni–YSZ anode material properties, microstructure, exchange current density i_o^a on triple phase boundary (TPB) and current density. The exchange current density i_o^a depends upon the H₂ partial pressure and the TPB length, which is itself influenced by the size and the number of electro-catalyst particles (Ni particles) per unit area very near the electrolyte surface. The loss of TPB length and porosity can be a major contribution of reducing the exchange current density. So the changes of Ni–YSZ microstructure and composition have a major influence on the activation polarization η_{act}^a. At constant current i, the activation polarization η_{act}^a increases with a decrease of the exchange current density i_o^a.

4.2. Thermodynamic and phase transition analysis

At 800 °C, the calculated thermodynamic phase diagram by FACTSAGE software shows that PH₃ can potentially react with Ni (Fig. 14). Under the cell working conditions, reactions (6)–(8) represent the three possible nickel phosphide products that can form in the cell anode. The changes of Gibbs free energy (ΔG) are negative values in these reactions at 800 °C (1073 K):

$$2PH_3(g) + 4Ni = 2Ni_2P(s) + 3H_2(g)$$
$$\Delta G(1073\,K) = -431.53\,kJ \qquad (6)$$

$$10PH_3(g) + 12Ni(s) = 2Ni_6P_5(s) + 15H_2(g)$$
$$\Delta G(1073\,K) = -1845.84\,kJ \qquad (7)$$

$$2PH_3(g) + 5Ni(s) = Ni_5P_2(s) + 15H_2(g)$$
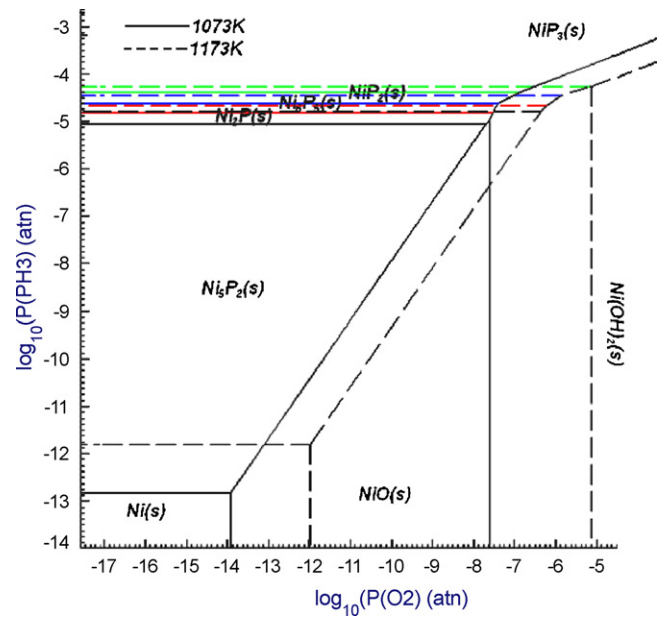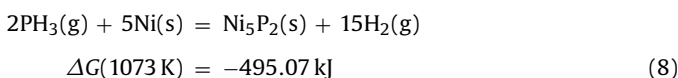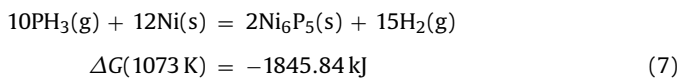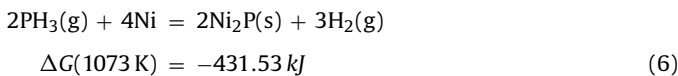$$\Delta G(1073\,K) = -495.07\,kJ \qquad (8)$$

Fig. 14. The thermodynamic phase diagram shows that 10 ppm (10^{-5} cm^{-3}) PH₃ impurity is potentially capable of reacting with Ni in the reducing environment.

The predominant phase diagram calculated by FACTSAGE in Fig. 14 indicates Ni₂P and Ni₆P₅ are the most favorable products at 800 °C for 10 ppm nominal concentration level of PH₃. As the cell operating temperature increases (due to current passage), Ni₅P₂ may also occur as a secondary phase. Further analysis revealed these nickel phosphide compounds can be in both solid and liquid states under the cell working conditions. The Ni–P phase diagram (Fig. 15) [20] shows that the solid–liquid phase transition temperature is as low as 800 °C for nickel phosphide with over 40% phosphorus atom concentration, which is the eutectic composition between Ni₂P and the intermediate phase Ni₅P₄ [19]. Under 0.5 A cm^{-2} current density loading, the local temperature of cell anode center can be 20 °C higher than the furnace temperature of
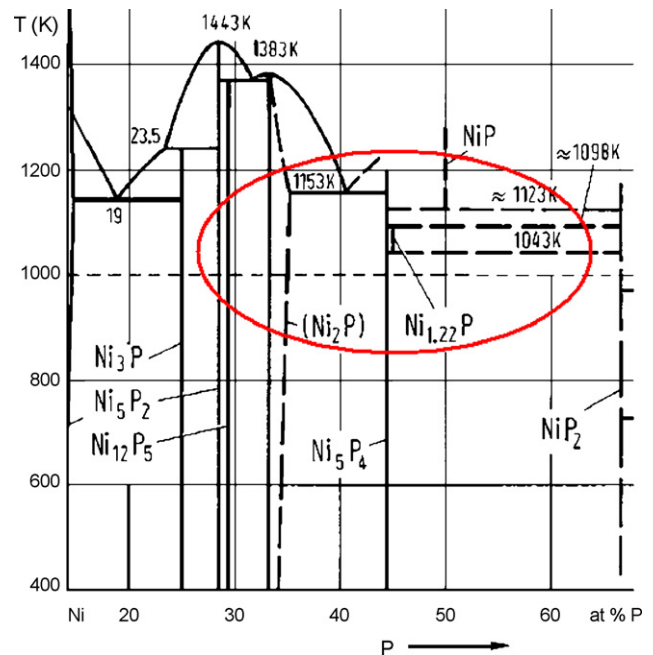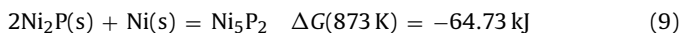

Fig. 15. P–Ni phase diagram. The cell working condition could fall well within the region marked by circle.

800 °C [21]. With 10 ppm PH_3 added continually to the cell surface over hundreds of hours, the phosphorus atom concentration at the center of anode surface could be high enough to liquefy nickel phosphide compound. The presence of a liquid nickel phosphide phase, most possibly Ni_2P in this case, explains how the nickel migrates to the cell anode surface and intrudes into the pore space inside the anode structure.

When the cell was cooled down from 1073 K to room temperature with N_2 purge, Ni_5P_2 was produced as a dominant nickel phosphide in the nickel rich and PH_3-absent environment:

$$2Ni_2P(s) + Ni(s) = Ni_5P_2 \quad \Delta G(873\,K) = -64.73\,kJ \tag{9}$$

$$2Ni_6P_5(s) + 13Ni(s) = 5Ni_5P_2 \quad \Delta G(873\,K) = -675.05\,kJ \tag{10}$$

This could explain that why Ni_5P_2 is detected as a major product on the PH_3-poisoned Ni–YSZ anode surface. The condition of the cell cooling may affect the presence of the final dominant nickel phosphide phase. Our finding of the phase Ni_5P_2 is distinct from Marina et al.'s report of Ni_3P as the product on Ni–YSZ anode exposed to syngas with 2 ppm PH_3 [8]. One possibility that could lead to the different findings is that our study uses an exposed Ni–YSZ anode center. If Ni mesh is placed at the anode center as current collector, the as-formed nickel phosphide liquid phase at cell operating temperature can readily migrate to the anode surface, and be reduced in situ by the excess Ni constituent to form Ni_3P [15].

Thermodynamic calculations at 300 K indicate that $Ni(OH)_2$ is the sole equilibrium phase for the Ni, P, O and H system under quite low H_2 partial pressure. However this calculation represents the case for complete system phase transition after a thermodynamically long period. At room temperature, such phase transitions may become kinetically very slow. Thus the N_2-quenching procedure may prevent most of the nickel phosphide formed at high temperature from transforming to nickel hydroxide. This hypothesis is supported by the XRD finding of Ni_5P_2 peaks. Additionally, more than one reaction path may still exist for the nickel phosphide phase transition. When the nickel phosphide at the anode surface is exposed to air and moisture at room temperature, the following reaction becomes thermodynamically quite favorable:

$$Ni_5P_2(s) + 5O_2(g) + 2H_2O(l) = Ni_3(PO_4)_2(s) + 2Ni(OH)_2(s)$$

$$\Delta G(300\,K) = -4104.6\,kJ \tag{11}$$
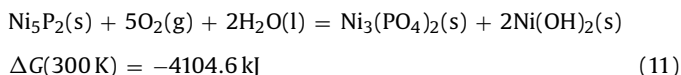
The XPS study does show formation of phosphate species on the anode surface, which can result from the transition of nickel phosphide to phosphate (Eq. (11)) under oxygen-rich condition. Similar XPS results have been reported in the literature [5,8]. However, this transition should be limited to a very superficial region due to slow kinetics, as it only initiates when the sample is totally cooled down and exposed to air at room temperature.

5. Conclusion

The long-term test of a Ni–YSZ anode-supported SOFC cell exposed to syngas with 10 ppm PH_3 impurity has been evaluated. Dramatic and irreversible degradation of cell performance (loss of voltage at constant current, increase in both ohmic and polarization resistance) is assigned to the functional deterioration of the Ni–YSZ anode, particularly the active layer near the electrolyte. According to thermodynamic analysis, nickel can react with phosphine

under these operating conditions and form liquid nickel phosphide phases. This mechanism is proposed to explain the migration of nickel particles to the exposed anode surface and agglomeration of nickel in the pores of the anode. Ni_5P_2 is identified as the major product. The changes of ohmic resistance and the polarization resistance are tentatively assigned to the nickel redistribution, most likely in the active composite layer next to the electrolyte. The polarization resistance increase can also be attributed to the loss of porosity and TBP length. While the investigation presented in this paper is based on 10 ppm PH_3 which may be more than is usually present in coal syngas, the results suggest that a lower PH_3 impurity concentration (e.g., ~2 ppm) in the coal-derived syngas may cause significant degradation of a Ni/YSZ anode on a time scale desired by DOE goals [1,2].

References

[1] J.P. Trembly, R.S. Gemmen, D.J. Bayless, J. Power Sources 163 (2007) 986–996.
[2] F.N. Cayan, M. Zhi, S.R. Pakalapati, I. Celik, N. Wu, R. Gemmen, J. Power Sources 185 (2008) 595–602.
[3] J.P. Trembly, Ph.D. Dissertation, Investigation into the effects of trace coal syn gas species on the performance of solid oxide fuel cell anodes, 2007.
[4] L.R. Pederson, O.A. Marina, X.-D. Zhou, Y.-S. Chou, G.W. Coffey, V.9 SECA Coal-Based Systems Core Research. V, Advanced Research, DOE FY 2007 Annual Report.
[5] M. Zhi, X. Chen, H. Finklea, I. Celik, N.Q. Wu, J. Power Sources 183 (2008) 485–490.
[6] F. Zhao, A.V. Virkar, J. Power Sources 141 (2005) 79–95.
[7] EG&G Services, Parson, Inc., and Science Applications International Corporation, Fuel Cell Handbook, 5th edition, U.S. Department of Energy, National Energy Technology Laboratory, Morgantown, WV, 2000.
[8] O.A. Marina, L.R. Petterson, D.J. Edwards, et al., Proceedings of the 8th SECA Workshop, San Antonio, TX, August, 2007.
[9] M. Yashima, S. Sasaki, M. Kakihana, Acta Crystallogr. Sect. B 50 (December) (1994) 663–672.
[10] G.S. Saini, L.D. Calvert, J.B. Taylor, Can. J. Chem. 42 (July (7)) (1964).
[11] M. Yousuf, P. CH. Sahu, H.K. Jajoo, S. Rajagopalan, K. Govinda Rajan, J. Phys., F 16F (1986) 373–378.
[12] D. Taylor, Trans. J. Br. Ceram. Soc. 83 (1984) 5.
[13] J.D. Hanawalt, H.W. Rinn, L.K. Frevel, Ind. Eng. Chem. Anal. Ed. 10 (9) (1938) 457–512.
[14] M.B. Pomfret, C. Stoltz, B. Varughese, R.A. Walker, Anal. Chem. 77 (2005) 1791.
[15] R.E. Dietz, G.I. Parisot, A.E. Meixner, Phys. Rev. B 4 (October (7)) (1971).
[16] H. Pfeiffer, F. Tancret, T. Brousse, Mater. Chem. Phys. 92 (2005) 534–539.
[17] C.D. Wagner, W.M. Riggs, L.E. Davis, J.F. Moulder, G.E. Muilenberg, Handbook of X-Ray Photoelectron Spectroscopy, PerkinElmer Corporation, Physical Electronics Division, Eden Prairie, MN, 1979, p. 55344.
[18] K.S. Kim, N. Winograd, Surf. Sci. 43 (2) (1974) 625–643.
[19] J.W. Kim, A.V. Virkar, K.Z. Fung, K. Mehtta, S.C. Singhal, J. Electrochem. Soc. 146 (1) (1999) 69–78.
[20] Konstantinov, Lee et al., Landolt-Bornstein, New Series IV/5, Ni–P, p. 1.
[21] S.C. Singhal, K. Kendall, ISSN 14710846 "High Temperature Solid Oxide Fuel Cells Fundamentals, Design and Applications", 1st edition, Elsevier Ltd., p. 280, 2003.
[22] J. Li, Y. Ni, K. Liao, J. Hong, J. Colloid Interf. Sci. 332 (1 April (1)) (2009) 231–236.